crystals

MDPI

Article

High-Temperature Phase Transformations in Al-Li-Cu-Mg-Zr-Sc Alloy Studied via In Situ Electron Microscopy

Rostislav Králík, Lucia Bajtošová, Barbora Kihoulou, Dalibor Preisler and Miroslav Cieslar *

Faculty of Mathematics and Physics, Charles University, Ke Karlovu 5, 12116 Prague, Czech Republic; rostislav.kralik@matfyz.cuni.cz (R.K.); lucibajtos@gmail.cz (L.B.); barbora.krivska@matfyz.cuni.cz (B.K.); dalibor.preisler@mff.cuni.cz (D.P.)
* Correspondence: miroslav.cieslar@mff.cuni.cz

Abstract: A homogenization of billets from Al-Cu-Li-Mg-Sc-Zr alloys should be accomplished at high annealing temperatures exceeding 500 °C. This type of aluminum alloy is susceptible to the depletion of surface layers from Li. Therefore, choosing a suitable homogenization temperature and duration is a crucial step in assuring a homogeneous distribution of alloying elements and optimal exploitation of the potential of the alloy. In situ heating in an electron microscope was performed on a twin-roll-cast Al-Cu-Li-Mg-Sc-Zr alloy to understand the peculiarities of the homogenization process. Four types of primary phase particles rich in Cu, Li, Mg, and Fe were identified in the as-cast material. They appear as coarse particles at the boundaries of eutectic cells. Their partial dissolution occurs at temperatures above 450 °C. They are almost fully dissolved at 550 °C, except for complex phases containing Fe and Cu. Small dimensions of eutectic cells in the range of 10 µm assure a homogeneous distribution of the main alloying elements within the matrix after 20 min of annealing at 530 °C. Direct comparison with the same material prepared by mold casting indicates that such short annealing times result in the dissolution of the main primary phase particles but do not assure a homogeneous distribution of the alloying elements in the whole volume of the specimen.

Keywords: Al-Cu-Li-Mg-Sc-Zr alloy; in situ TEM; homogenization; primary phase particles; twin-roll casting; mold casting

Citation: Králík, R.; Bajtošová, L.; Kihoulou, B.; Preisler, D.; Cieslar, M. High-Temperature Phase Transformations in Al-Li-Cu-Mg-Zr-Sc Alloy Studied via In Situ Electron Microscopy. *Crystals* **2024**, *14*, 136. https://doi.org/10.3390/cryst14020136

Academic Editors: Daniel Medyński, Grzegorz Lesiuk and Anna Burduk

Received: 13 January 2024
Revised: 25 January 2024
Accepted: 26 January 2024
Published: 29 January 2024

1. Introduction

Al-Cu-Li-Mg-based alloys are promising materials that are extensively used in aerospace components thanks to their superior mechanical properties and good corrosion resistance. The Li addition secures the low density and high elastic modulus of the materials [1,2]. In the case of the newest generation of Al-Li-based alloys, only a reduced concentration of Li (0.75 to 1.8 wt. %) is kept [3]. Earlier generations of Al-Li-based materials relied on higher Li concentrations and the formation of metastable δ′ Al_3Li precipitates [4]. However, those precipitates were found to be easily shearable during deformation and responsible for anisotropic material properties and poor fatigue performance [5]. The current generation of Al-Li-based alloys favors the formation of other strengthening phases by adding more alloying elements and the formation of ternary strengthening phases. In Al-Li-Cu alloys, they are primarily Cu-based phases—mainly the binary θ′ (Al_2Cu) and ternary T_1 (Al_2CuLi) [6,7]. The tetragonal θ′ forms on {100} planes of the Al matrix while the hexagonal T_1 phase forms on the {111} planes, offering complementary strengthening and further improvement in isotropy compared to the binary Al-Li alloys. The hexagonal T_1 precipitates form preferably in the grain and subgrain boundaries or pseudo-hexagonal areas of stacking faults in the FCC matrix. However, the stacking fault energy in Al is high, and the lifetime of extended dislocations is too short to ensure a sufficient density of nucleation sites. Therefore, precipitation of T_1 can be further stimulated by adding alloying elements such as Ag or Mg, which reduce the stacking fault energy, retard recovery, and, as a consequence, promote a more homogeneous distribution of precipitates of the T_1 phase inside grains [8]. A further advantage of Mg addition is a decrease in the total density of the material and precipitation of a rod-like strengthening S′ (Al_2CuMg) phase [9].

Recrystallization, texture control, and fatigue improvement are achieved by adding Zr, or Zr and Sc, which form fine Al_3Zr or $Al_3(Zr, Sc)$ dispersoids [10]. On the other hand, the presence of Fe impurities in the input materials generally leads to the formation of an insoluble constituent Al_7Cu_2Fe phase [11].

Conventional methods of sheet production from the Al-Cu-Li-Mg-based alloys start with the employment of ingot-casting methods such as direct-chill (DC) casting, vacuum induction casting (VIC), or mold casting (MC) under a protective atmosphere. Ingot-cast materials exhibit an inhomogeneous solute distribution on a macroscopic level, contain coarse constituent particles, and form large eutectic cells. Dissolving the coarse particles and homogeneous distribution of the constituent elements is necessary to achieve the peak mechanical properties from the phases precipitated during the final age hardening. For this reason, homogenization annealing should follow the casting of the material before the multi-step hot forming, solution treatment, and age hardening are accomplished [12–14].

Long-term homogenization at high annealing temperatures is required for homogenization and primary phase dissolution. Temperatures between 500 °C and 530 °C are specified as a standard for homogenizing this type of alloy [15–18]. However, a multi-step homogenization treatment is often used with the first steps at temperatures below 500 °C. Suresh and Sharma [15] performed the homogenization annealing of a mold-cast AA2195 at 470 °C/16 h and 500 °C/8 h. Nayan et al. [18] used a three-step homogenization at 435 °C/8 h, 495 °C/12 h, and 525 °C/32 h. The choice of the scheme is based on thermal measurements. Low-temperature annealing should protect the alloy from a detrimental local melting of primary phases with low melting points. The final long-term annealing at a high temperature then ensures the dissolution of the remaining primary phases and a homogeneous distribution of the main alloying elements in the whole volume of the original eutectic cells.

However, in the case of Al-Li-based alloys, such long-term high-temperature annealing induces the evaporation of Li from the surface [19] and the formation of Li-depleted layers. Scalping of Li-depleted surface layers is then necessary and generates a considerable amount of waste. While this scrap could be partially reused using special scrap-treatment procedures, this processing would be critically detrimental in strip-cast materials, where scalping would cause high volume losses of the cast material.

Moreover, fine Sc-containing dispersoids, which generally form between 300 and 480 °C, are prone to coarsening at standard homogenization temperatures [20] and lose their advantageous effects once they coarsen beyond the coherency limit. This coarsening could be significantly suppressed in alloys micro-alloyed with Sc and Zr due to the synergistic effect between the two elements [13]. Both the nanoscale Al_3Zr metastable phase and the Al_3Sc phase have the same $L1_2$ structure [21]. However, the diffusivity of Zr is lower than the diffusivity of Sc in Al. Therefore, the Al_3Zr phase precipitates at higher annealing temperatures, forming a complex core–shell $Al_3(Sc,Zr)$ phase. The Zr-rich shell forms even at low Zr concentrations, which impedes the later stages of particle transformation, making the ternary phase more resistant to coarsening than the binary AlSc precipitate [22]. Still, some $Al_3(Zr, Sc)$ dispersoid growth was consistently observed, even at relatively low annealing temperatures (<500 °C) [23,24]. While precipitation of the nanoscale Al_3Sc is intended when adding Sc to Al alloys, the precipitation of coarse AlCuSc primary phases is also possible. DePottey et al. [25] propose a mechanism of the Sc enrichment of primary θ phase sites, which leads to the precipitation of the primary W phase ($Al_{8-x}Cu_{4+x}Sc$ where $0 < x < \approx 2.15$). This phase forms at cooling rates between 0.1 $K{\cdot}s^{-1}$ and 10 $K{\cdot}s^{-1}$, commonly associated with ingot-casting methods. This phase is considered detrimental because it further depletes the material from the valuable Sc, further highlighting the poor compatibility of Sc addition to ingot-cast materials.

Alternative methods of thin strips or thick sheets of the Al-Cu-Li-Mg-Zr-based material preparation can be employed to reduce the duration of homogenization at high temperatures, comprising continuous casting methods, also including twin-roll casting (TRC). The molten material is poured through a narrow gap onto water-cooled rolls during TRC, solidifying and undergoing a short hot forming. While TRC has been chiefly used in low-alloyed systems with a narrow solidification range, several TRC castings of Al-Li-based materials are promising [26,27]. Due to high solidification rates related to this method, much finer primary constituent particles are formed, and the segregation scales are much lower. Consequently, solute homogenization and primary phase dissolution are possible at significantly shorter annealing times, diminishing the undesirable effects of the homogenization annealing of ingot-cast materials, namely the coarsening of Al_3(Sc, Zr) dispersoids and Li surface evaporation.

In this work, specimens of a TRC Al-Cu-Li-Mg-Zr-Sc alloy were annealed in situ in a scanning transmission electron microscope (STEM). The transformation of primary phase precipitates and the precipitation and dissolution of other secondary phases during the experiment were closely monitored. Comparison with mold-cast material of identical composition was carried out, including the phase analysis directly at selected annealing temperatures using automated crystal orientation mapping (ACOM-TEM).

2. Materials and Methods

An alloy with the composition given in Table 1 was used as the input material for preparing the TRC and MC materials. The input material was manufactured using commercial AA2195 aluminum alloys and an Al-2wt.% Sc master alloy. The concentrations of respective elements shown in Table 1 represent the average values received from three measurements on both the TRC and MC billets. The TRC material was poured at a temperature of 660 °C with a casting rate of 3.6 $\mathrm{m \cdot min^{-1}}$. The furnace, the tundish with a ceramic nozzle, and the roll gap were all flooded with Ar to avoid exothermic oxidation of lithium. The molten alloy was mechanically stirred by BN-coated blades to avoid the gravitational segregation of Sc. The roll-separating force was approximately 200 kN during the casting process. The final cast strip was 3 mm thick and 20 mm wide—the barrel length of the caster rolls [28].

Table 1. Average composition of TRC and MC materials in wt.

Element	Cu	Li	Mg	Zr	Sc	Ag	Ti	V	Fe	Al
Concentration	2.60(8)	0.71(8)	0.27(2)	0.12(6)	0.16(4)	0.24(7)	0.01(1)	0.01(1)	0.10(6)	bal.

MC was performed under an argon protective atmosphere to an air-cooled graphite mold of 110 × 56 × 26 mm^3. Irregularities and surface impurities of the ingots were scalped to obtain a final block 85 × 50 × 22 mm^3, which was used for further processing and study. The chemical composition of both alloys was received from optical emission spectrometry (Q4 TASMAN).

Slices of both materials cut by SiC discs were mechanically ground on SiC papers to a thickness of 100 µm, and 3 mm discs were punched out of these slices. The final electrolytic polishing in a twin-jet TENUPOL V with a 33 % solution of HNO_3 in methanol was performed at −16 °C. Transmission electron microscopy and scanning transmission electron microscopy (TEM/STEM) observations, and scanning electron microscopy (SEM) were performed in a JEOL JEM 2200 FS electron microscope in TEM, STEM, and SEM modes using bright field (BF), high-angle annular dark field (HAADF), and back-scattered electron (BSE) modes with a 200 kV acceleration voltage. The Gatan heating stage for TEM was used for step-by-step in situ heating with an average step of 50 °C/20 min. Energy-dispersive spectroscopy (EDS) characterizations of the initial and annealed TRC specimens were performed at room temperature (annealed specimens were cooled to room temperature in the TEM heating stage with a cooling rate of 200 °C/min) using the Jeol

Centurio Large Angle SDD detector (JEOL, Tokyo, Japan). The TEM is equipped with "Spinning Star" electron precession from NanoMEGAS with an ASTAR DigiStar Control version 1.4 software package for the automated crystal orientation mapping (ACOM-TEM) and the acquisition of phase maps.

Due to the size of eutectic cells in the MC material exceeding standard TEM magnifications, the microscope was operated in a low magnification mode in STEM during the insitu experiment. However, this mode does not allow for the use of the EDS detector. Therefore, the initial and post-mortem observations of the MC material, EDS mapping, and BSE observations were performed in the FEI Quanta 200F SEM on the same specimen. A 20 kV acceleration voltage in combination with a 10 mm working distance from the pole piece was used to obtain the optimal signal for EDS mapping. EDAX Genesis software version 6.531 was used to acquire and evaluate the SEM-EDS maps.

3. Results

3.1. As-Cast Structures

Because the high-temperature behavior of ingot-cast Al-Li alloys is well described in the literature [12–14], only brief characterizations were performed in the present study. The microstructure of the MC material consists of polyhedral eutectic cells with particles of primary phases at their boundaries. Figure 1 shows typical SEM images and EDS maps of the main alloying elements in the material. Coarse Cu-rich primary phase particles are located along the boundaries of the eutectic cells. The detected chemical composition indicates the presence of θ-Al_2Cu or T_1-Al_2CuLi phases. The presence of Mg could not be reliably excluded because the local concentrations in particles are very similar to the ones in the bulk of the material. The S-Al2CuMg phase is probably also present in the eutectic cell boundaries. An increased concentration of Cu is apparent in an approximately 10 μm broad area around the primary phases (Figure 1c—white arrows). This concentration gradient between the grain boundary and its interior appears as a direct effect of the eutectic solidification of the alloy [29]. Additionally, smaller (below 5 μm) Fe-rich particles, most probably of the Al_7Cu_2Fe phase [30], appear in several parts of the boundary of the eutectic cell (Figure 1d).

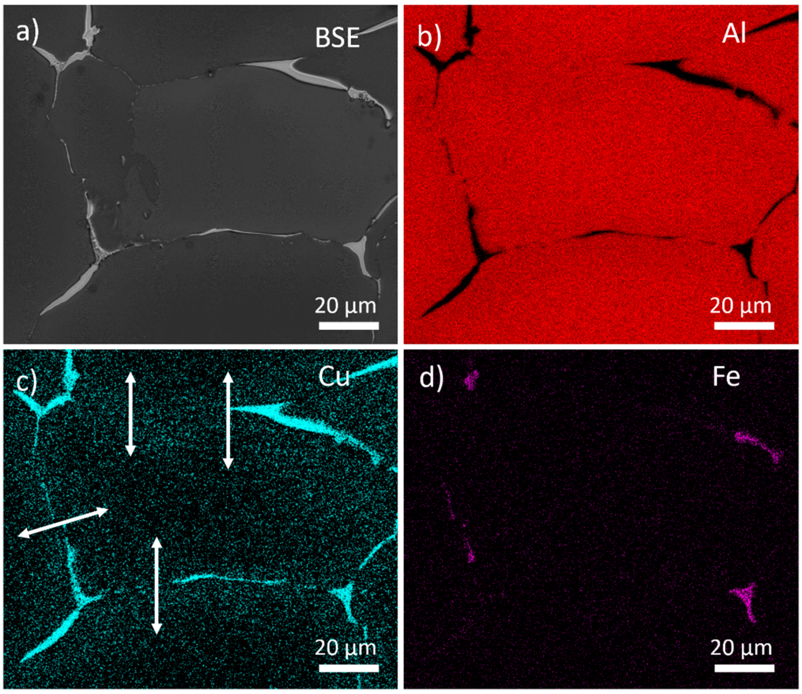

Figure 1. Distribution of elements in as-cast MC alloy. SEM BSE image of the primary phases (**a**). Corresponding EDS maps (**b**–**d**).

Generally, as-cast TRC materials exhibit a finer cell size, finer dispersion of primary particles, and higher solid solution supersaturation [31]. Figure 2 shows two examples of boundary particles in a thicker part of the TEM specimen (~500 nm). The noticeable gradient in the Cu concentration observed in the MC material (Figure 1c) is not evident in the TRC material (Figure 2c,h). The brighter part (higher intensity of inelastically scattered electrons) near particles in the HAADF contrast (Figure 2a,f) represents only parasitic thickness modifications due to the inhomogeneous distribution of potentials during the electropolishing of the specimen. Nevertheless, an elevated concentration of Mg in several rod-like particles suggests the presence of the S-Al_2CuMg phase.

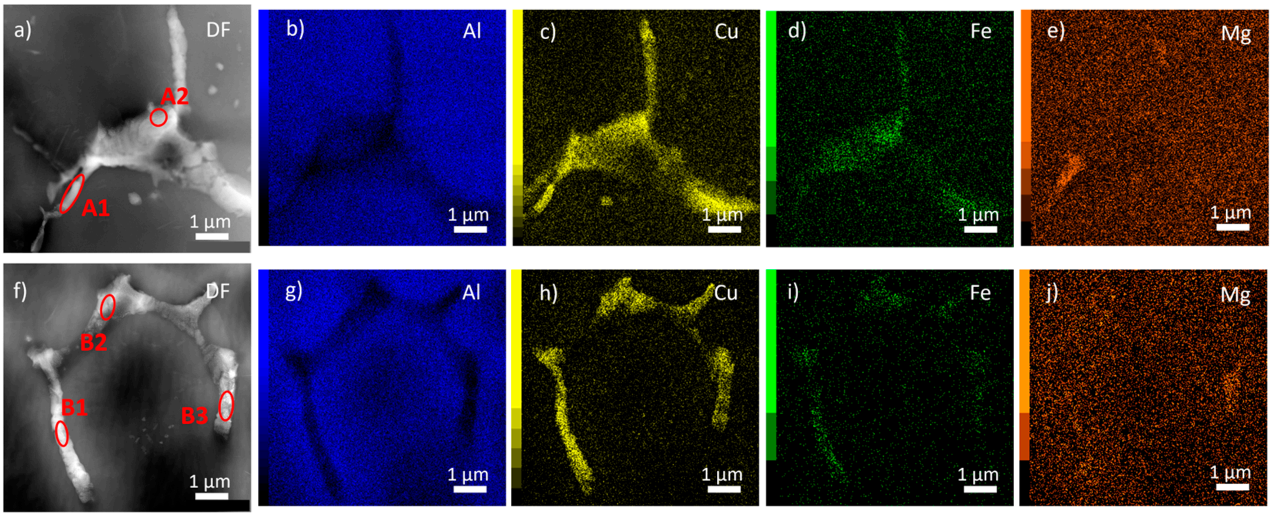

Figure 2. Distribution of main alloying elements in the as-cast TRC alloy. HAADF STEM images (**a**,**f**). Corresponding EDS maps (**b**–**e**,**g**–**j**).

Quantification of the composition was performed in several parts of the primary phase particles. Examples are listed in Table 2. Because there is always an overlap of several particles containing Al, Cu, Mg, and Fe, Li cannot be detected by EDX, and particles are embedded in the Al matrix, a direct interpretation of the measured concentration is impossible. However, higher concentrations of Cu, Fe, and Mg suggest the existence of big equilibrium θ-Al_2Cu, T_1-Al_2CuLi, or S-Al_2CuMg phases overlapped with smaller particles of the Al_7Cu_2Fe phase (concentrations of other elements fell below 0.1 at. %). Statistical diffraction analysis of the particles in thinner parts of the specimen using ACOM-TEM proves the presence of θ, S, and T_1 particles (examples in Figures 3–5) in the as-cast state. More details about this type of analysis can be found in the work of Bajtošová et al. [32].

Table 2. Concentrations of elements in selected spots of the as-cast TRC material (at. %).

Area	Al	Cu	Fe	Mg
A1	75.4	23.4	0.1	1.2
A2	74.6	23.9	1.0	0.6
B1	47.2	51.1	1.3	0.4
B2	63.6	35.5	0.6	0.3
B3	56.9	35.9	1.4	5.8

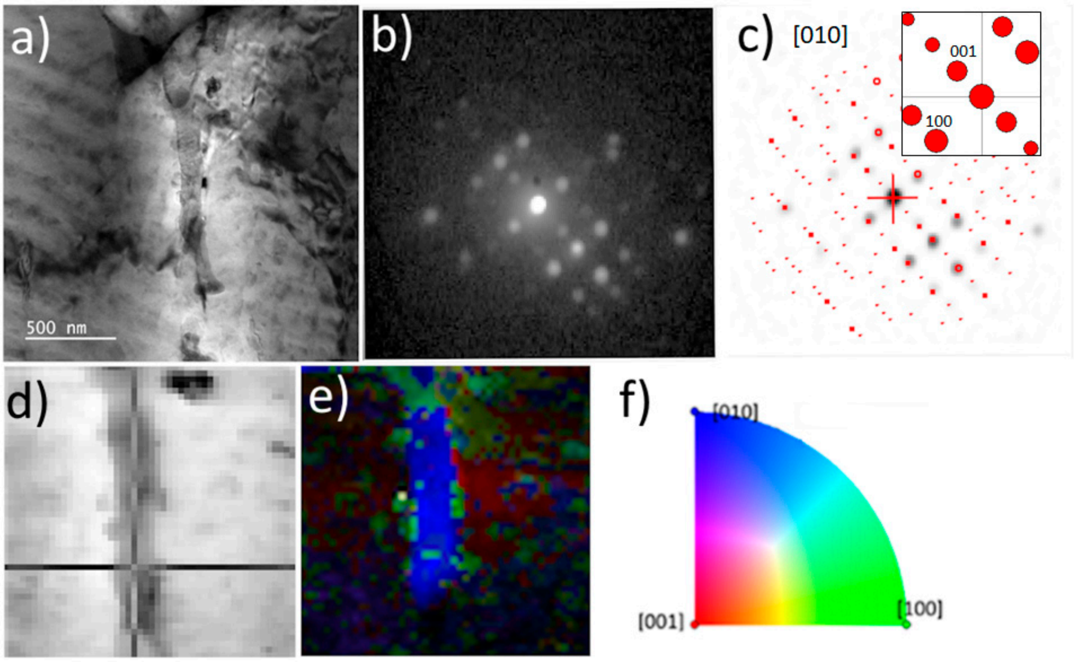

Figure 3. ACOM-TEM analysis of primary centered orthorhombic S-Al_2CuMg phase in as-cast TRC alloy. TEM BF image (**a**), experimental diffraction pattern (**b**) and matching with simulations (**c**), virtual BF (**d**) indicating the acquisition position of the diffraction pattern in (**c**), orientation map (**e**), orientation triangle (**f**).

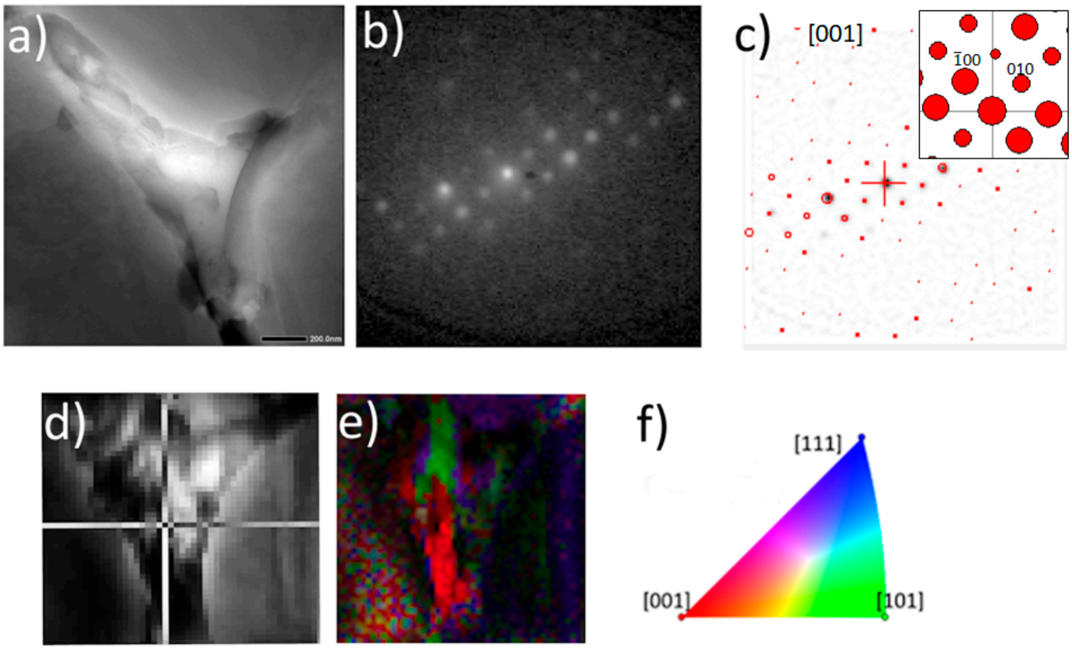

Figure 4. ACOM-TEM analysis of primary body-centered tetragonal θ-Al_2Cu phase in as-cast TRC alloy. TEM BF image (**a**), experimental diffraction pattern (**b**) and matching with simulations (**c**), virtual BF (**d**) indicating the acquisition position of the diffraction pattern in (**c**), orientation map (**e**), orientation triangle (**f**).

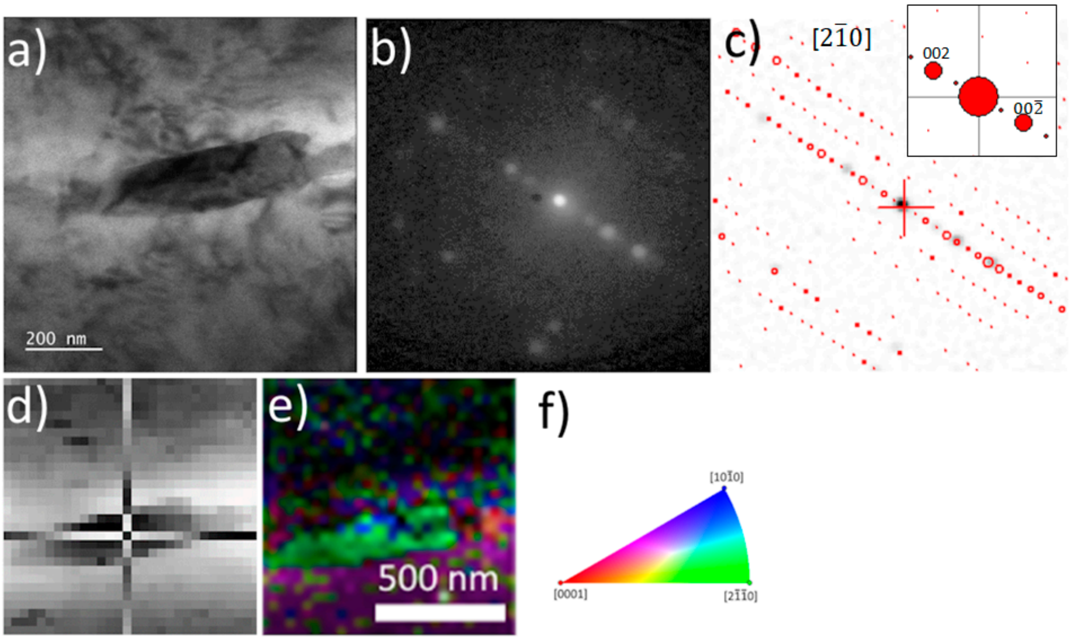

Figure 5. ACOM-TEM analysis of primary hexagonal T_1-Al_2CuLi phase in as-cast TRC alloy. TEM BF image (**a**), experimental diffraction pattern (**b**) and matching with simulations (**c**), virtual BF (**d**) indicating the acquisition position of the diffraction pattern in (**c**), orientation map (**e**), orientation triangle (**f**).

3.2. In Situ Annealing

Specimens for this type of measurement were fixed first in the heating stage of the TEM and then step-by-step annealed to the final high temperatures. A back-scattered electron detector in the low magnification SEM mode in the MC alloy was used. The processes in Figure 6 are similar to those observed generally in ingot-cast materials [12]. Primary phase particles remain almost uninfluenced by the annealing up to 500 °C. However, the majority of them rapidly dissolve at 560 °C.

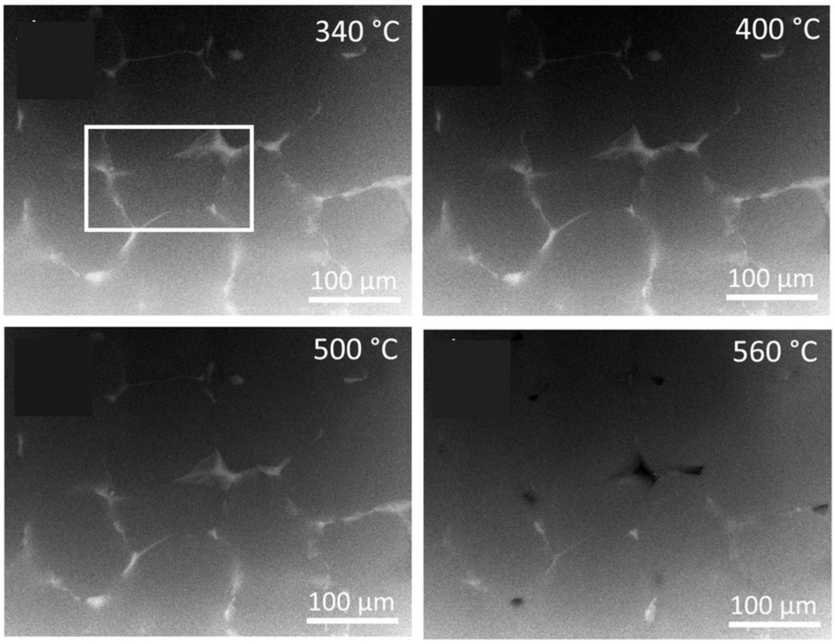

Figure 6. In situ SEM annealing in the stepwise regime of 50 °C/20 min of MC specimen, BSE detector signal. The white rectangle indicates the area analyzed in the as-cast state by SEM (Figure 1).

Closer EDX and SEM analyses (Figure 7) were performed on the same specimen zone as in Figure 1. The specimen was cooled to room temperature first. A relatively low cooling rate (200 K/min) does not preserve the structure formed at high temperatures, and the material exhibits another feature typical for ingot-cast Al-Li-Cu-Mg alloys exposed to elevated temperatures for relatively short times (~20 min at 560 °C). While only insoluble Cu and Fe-rich particles (most probably Al_7Cu_2Fe) persist, a part of the Cu atoms near the original boundaries of the eutectic cells reprecipitate in the coarse Cu-rich particles (marked by arrows in Figure 7a). According to the literature [29], this limited zone confirms that a homogeneous distribution of Cu could not be reached in ingot-cast materials containing relatively large eutectic cells during such a short annealing period. The material was exposed to standard homogenization temperatures (>500 °C) for approximately 30 min before the in situ annealing experiment ended.

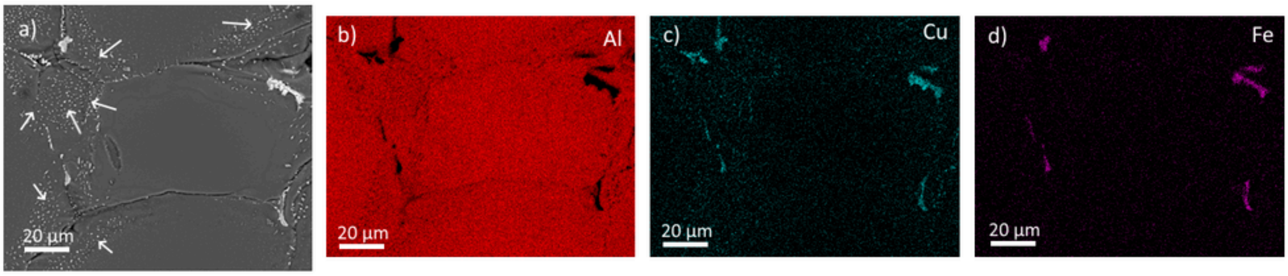

Figure 7. (**a**) SEM BSE image of the highlighted MC specimen area after in situ annealing up to 560 °C and cooling to room temperature, (**b**–**d**) EDS maps.

Primary phase particles in the TRC material are significantly finer than in the MC alloy. Their distribution in smaller eutectic cells strongly impacts the redistribution of the main alloying elements during annealing. The evolution of the two particles from Figure 2 during this process is displayed in Figures 8 and 9. Only the precipitation and coarsening of common strengthening nanoscale precipitates known for this system [33,34] occur at temperatures up to 300 °C. The first signs of the segmentation of the original particles occur at 400 °C—a much lower temperature than that of the MC specimen. It is accompanied by a coarsening of the matrix precipitates near the boundaries of the eutectic cells, most probably due to the elevated concentration of solute atoms released from the boundary particles during the segmentation. A substantial dissolution of the matrix particles begins above 450 °C, similar to the dissolution of the primary phase particles. However, due to the size of the primary phase particles, their decomposition is finalized at 500 °C. Above this temperature, most boundary phases are dissolved, and the remaining ones go through visible morphological modifications connected with their coalescence and ripening.

Figure 10 illustrates the detailed dissolution of one Al_2CuLi primary phase particle in a thinner part of the specimen and the formation of smaller matrix particles at temperatures close to 400 °C and 450 °C. In contrast to EDX characterization, ACOM-TEM analysis is not limited by the elevated temperature. The only limitation is the quality of the diffraction pattern, which might considerably depend on the thickness of the TEM foil and the overlap of several phases. The original Al_2CuLi particle, stable at 400 °C, dissolves at 450 °C and is substituted by stable matrix precipitates even after cooling to room temperature.

Figure 11 and Table 3 show that only complex phases containing Cu and Fe (Al_7Cu_2Fe) remain after annealing at 550 °C and cooling to room temperature. Coarse particles enriched in Cu (D1) or Mg (D3) in Figure 11f appear as an artifact of a limited cooling rate because they do not exist at high temperatures (Figures 8 and 9).

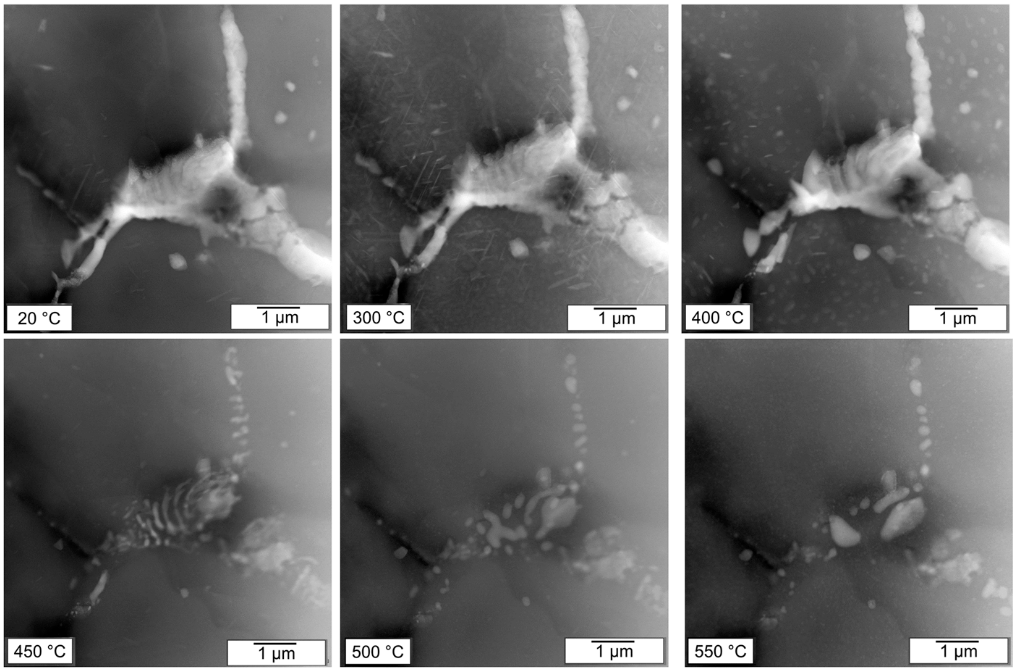

Figure 8. Evolution of primary phase particles in TRC material during in situ heating in the stepwise annealing regime of 50 °C/20 min. STEM HAADF images.

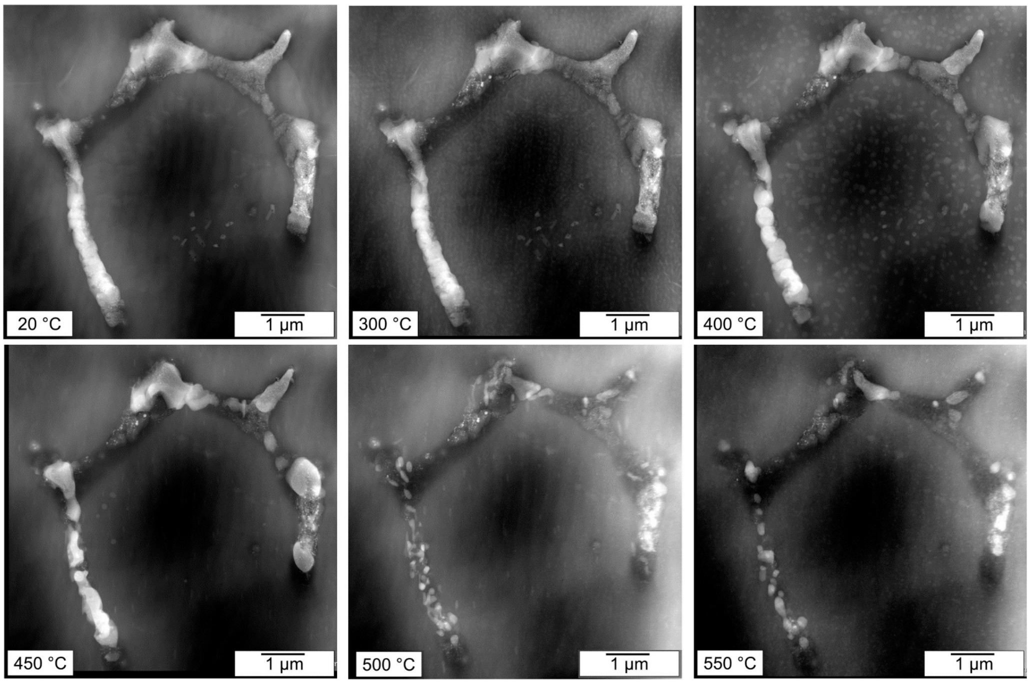

Figure 9. HAADF micrographs of the TRC alloy during an in situ annealing experiment with a 50 °C/20 min heating step.

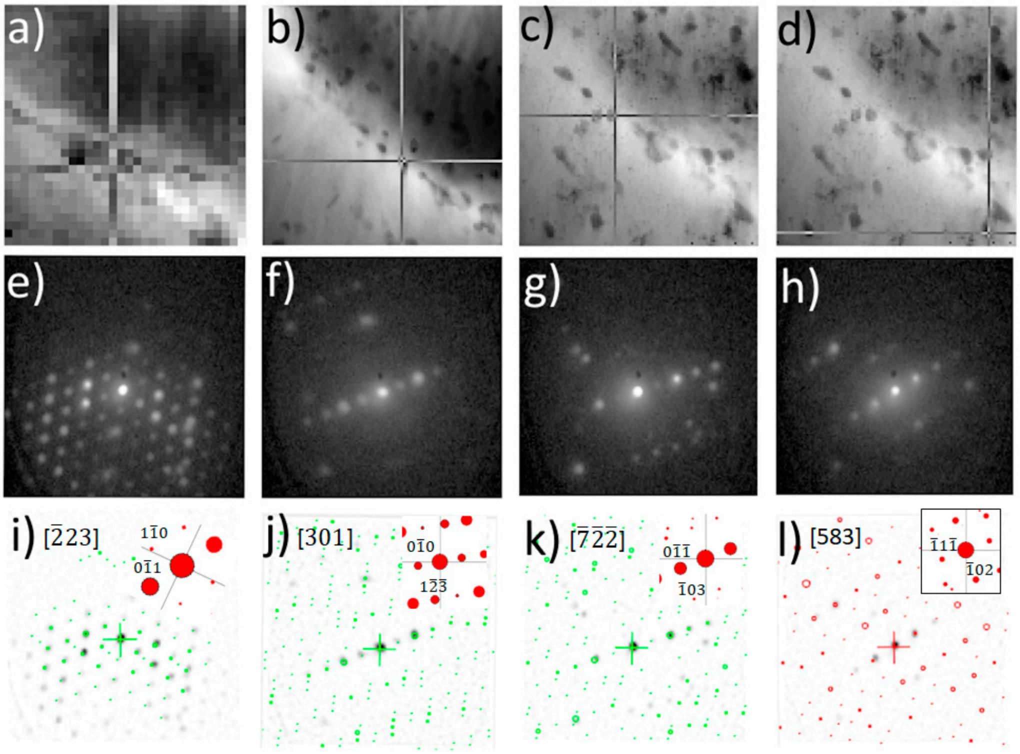

Figure 10. ACOM-TEM analysis of dissolution of primary Al_2CuLi particle. Virtual bright field (**a**–**d**), corresponding diffractograms (**e**–**h**), and automated phase matching (**i**–**l**). Al_2CuLi primary phase particle (**a**,**e**,**i**), Al_2CuLi precipitates (**b**,**c**,**f**,**g**,**j**,**k**), and Al_2Cu precipitate (**d**,**h**,**l**). Temperature of 400 °C (**a**,**e**,**i**), 450 °C (**b**,**f**,**j**), and room temperature (**c**,**d**,**g**,**h**,**k**,**l**).

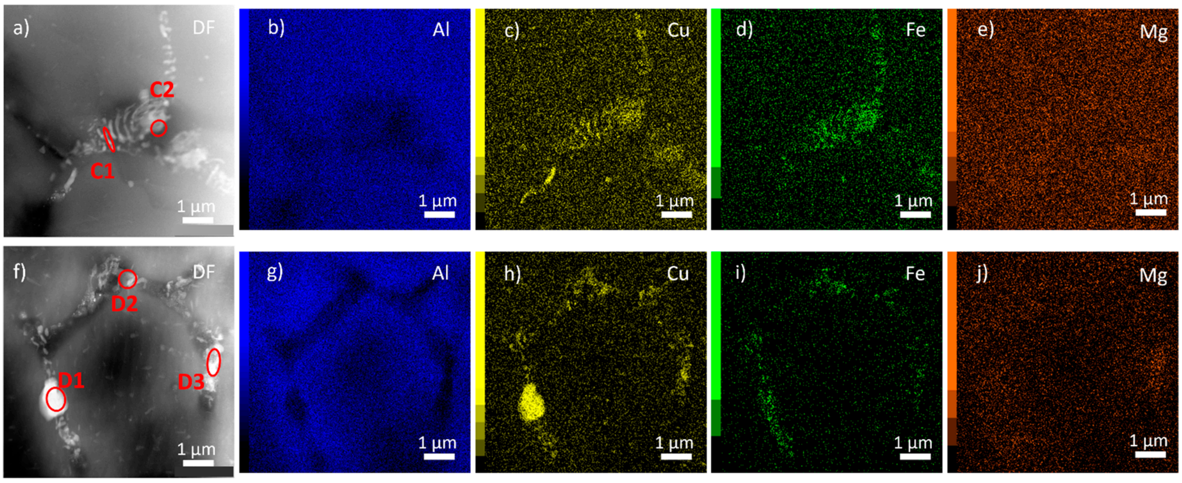

Figure 11. TRC material after annealing up to 550 °C and cooling to room temperature. HAADF STEM images (**a**,**f**) and corresponding EDS maps of main alloying elements (**b**–**e**,**g**–**j**).

Table 3. The concentration of elements in selected spots of the in situ annealed TRC material cooled to room temperature (at. %).

Area	Al	Cu	Fe	Mg
C1	88.8	9.7	1.1	0.5
C2	90.4	6.8	1.8	1.0
D1	46.9	51.2	0.9	1.0
D2	75.8	19.7	2.8	1.8
D3	72.4	20.4	1.0	6.2

4. Discussion

The twin-roll casting of Al-Li-based strips could provide properties not achievable via conventional ingot-casting and downstream processing methods due to significantly higher solidification rates reaching 10^2–10^3 K/s [35] compared to units of K/s typical for DC-cast Al alloys [36]. Although the cooling rate in TRC materials is relatively high, eutectic cells with coarse primary phase particles always form, and homogenizing the material at high temperatures is unavoidable. The critical parameter controlling the temperature and duration of this homogenization treatment is the size of the eutectic cells or dendrite secondary arm spacing L [27,37]. Generally, they are related to the cooling rate v_c or a local solidification time t_s by a power function [38,39]:

$$L = A \cdot v_c^{-n} \tag{1}$$

$$L = B \cdot t_s^n \tag{2}$$

where n is an empirical factor ranging from 1/3 to 1/2, and A and B are material-dependent constants. Rough estimations yield the ratio between the cell sizes of the TRC alloy and MC alloy ranging between 5 and 20, which is in good agreement with the structures of our materials (compare Figures 1 and 2).

The insitu TEM experiment shows that for a complete dissolution of the equilibrium θ-(Al_2Cu), T_1-(Al_2CuLi), and S-(Al_2CuMg) phases, the homogenization temperature should approach 550–560 °C in agreement with the literature data, while the Fe-bearing phase Al_7Cu_2Fe persists [12,13,27,36]. This temperature transfers the majority of the main solute atoms from the cell boundary into the matrix. However, short annealing times in the range of tens of minutes do not guarantee their homogeneous distribution in the original eutectic cell. The diffusion length w is defined from the diffusion coefficient D as

$$w = (Dt)^{\frac{1}{2}} \tag{3}$$

where t is the annealing time, and

$$D = D_0 \exp\left(-\frac{Q}{RT}\right) \tag{4}$$

is, for the slowest element (Cu), about 5 µm at 550 °C and 20 min ($D_0 = 4.8 \times 10^{-5}$ m^2/s, $Q = 133.6 \times 10^3$ J/mol, $R = 8.314$ J/(mol·K), and T is the thermodynamic temperature) [12]. This distance corresponds well with the width of the precipitation zone in the MC specimen cooled from the homogenization temperature to room temperature (Figure 7a). The TRC material does not exhibit such well-delimited precipitation zones. The characteristic dimension of the eutectic cell is of the same range as the diffusion length. Therefore, precipitates formed in the cooled specimen (Figure 11f) are homogeneously spread in the whole volume of the original eutectic cell. Longer homogenization duration is necessary for a homogeneous distribution of solutes in the MC material. Estimations based on Equation (3) yield a duration time close to 10 h to guarantee the diffusion length above 25 µm. This value is close to one-half of the eutectic cell size in the MC alloy.

5. Conclusions

The Al-Cu-Li-Mg-Sc-Zr-based alloy prepared via two methods with vastly different solidification rates was investigated during a model in situ homogenization experiment in TEM. A multi-step heat treatment of the strip using relatively short exposures at high temperatures is proposed. This treatment consists of annealing at 300 °C/30 min, 450 °C/30 min, and 530 °C/30 min. The first two steps should ensure the formation of Sc-rich precipitate cores and Zr-rich outer shells, respectively. The final step serves as a homogenization/solution treatment.

The following conclusions can be deduced from the present study:

- A high solidification rate during twin-roll casting impacts the size of the eutectic cells. Their average diameter is in the range of several micrometers. The mold-cast material exhibits a larger cell size by one order of magnitude.
- The primary phase particles situated at the cell boundaries were identified by ACOM-TEM and EDX analyses as θ-(Al_2Cu), T_1-(Al_2CuLi), S-(Al_2CuMg), and Al_7Cu_2Fe.
- The Al_7Cu_2Fe phase cannot be dissolved during the homogenization annealing. Only indistinctive morphological changes and ripening occur at temperatures above 500 °C.
- The remaining primary phase particles dissolve in both materials after 20 min holding time at temperatures close to 550 °C. The duration of this annealing is sufficient to distribute the main alloying elements homogeneously in the original eutectic cells in the TRC material. A couple of tens of hours of homogenization times would be necessary to receive the same homogeneous distribution in the MC material.
- The observed processes are in good agreement with recent diffusion models.

Author Contributions: Conceptualization: M.C.; investigation: L.B., R.K., B.K. and D.P.; supervision: M.C.; visualization: L.B. and R.K.; writing—original draft: R.K. and L.B.; writing—review and editing: R.K. and M.C. All authors have read and agreed to the published version of the manuscript.

Funding: This research was funded by the Czech Science Foundation project number 20-19170S and the Charles University Grant Agency project number 938120.

Institutional Review Board Statement: Not applicable.

Data Availability Statement: The original contributions presented in this study are included in the article. Further inquiries can be directed to the corresponding author.

Acknowledgments: The authors would like to acknowledge the assistance of Olexandr Grydin, Mirko Schaper, and Mykhailo Stolbchenko in manufacturing and providing the twin-roll cast materials.

Conflicts of Interest: The authors declare no conflicts of interest.

References

1. Prasad, N.; Gokhale, A.; Rao, P. Mechanical behavior of aluminium-lithium alloys. *Mat. Sci. Eng.* **2003**, *28*, 209–246. [CrossRef]
2. Starke, E.A.; Staley, J.T. Application of modern aluminum alloys to aircraft. *Prog. Aerosp. Sci.* **1996**, *32*, 131–172. [CrossRef]
3. Rioja, R.J.; Liu, J. The Evolution of Al-Li Base Products for Aerospace and Space Applications. *Metall. Mater. Trans. A* **2012**, *43*, 3325–3337. [CrossRef]
4. Flower, H.; Gregson, P. Solid state phase transformations in aluminium alloys containing lithium. *Mater. Sci. Technol.* **1987**, *3*, 81–90. [CrossRef]
5. Venkateswara Rao, K.T.; Ritchie, R.O. Fatigue of Aluminum-Lithium Alloys. *Int. Mater. Rev.* **1992**, *37*, 153–185. [CrossRef]
6. Meetsma, A.; Deboer, J.L.; VanSmaalen, S. Refinement of the crystal structure of tetragonal Al_2Cu. *J. Solid State Chem.* **1989**, *83*, 370–372. [CrossRef]
7. Noble, B.; Thompson, G.E. T1 (Al2CuLi) Precipitation in Aluminium–Copper–Lithium Alloys. *Met. Sci. J.* **1972**, *6*, 167–174. [CrossRef]
8. Wang, S.C.; Starink, M.J. Precipitates and intermetallic phases in precipitation hardening Al–Cu–Mg–(Li) based alloys. *Int. Mater. Rev.* **2005**, *50*, 193–215. [CrossRef]
9. Heying, B.; Hoffmann, R.-D.; Pottgen, R. Structure Refinement of the S-Phase Precipitate $MgCuAl_2$. *Z. Naturschoft.* **2005**, *60*, 491–494. [CrossRef]
10. Tolley, A.; Radmilovic, V.; Dahmen, U. Segregation in Al3(Sc,Zr) precipitates in Al–Sc–Zr alloys. *Scr. Mater.* **2005**, *52*, 621–625. [CrossRef]
11. Yu, C.; Yin, D.; Zheng, F.; Yu, X. Effects of solution treatment on mechanical properties and microstructures of Al-Li-Cu-Mg-Ag alloy. *J. Cent. South Univ.* **2013**, *20*, 2083–2089. [CrossRef]
12. Huang, H.; Xiong, W.; Jiang, Z.; Zhang, J. A Quasi In-Situ Study on the Microstructural Evolution of 2195 Al-Cu-Li Alloy during Homogenization. *Materials* **2022**, *15*, 6573. [CrossRef] [PubMed]
13. Tang, Y.; Xiao, D.; Huang, L.; You, R.; Zhao, X.; Lin, N.; Ma, Y.; Liu, W. Effect of Minor Sc Addition on the Microstructure Evolution of Al–Cu–Li–Mg Alloy During Homogenization with Different Cooling Modes. *Met. Mater. Int.* **2022**, *28*, 2422–2433. [CrossRef]
14. Yang, S.; Jian, S.; Xiaodong, Y.; Xiwu, L.; Fei, Z.; Baoging, S. Homogenization Treatment Parameter Optimization and Microstructural Evolution of Al-Cu-Li Alloy. *Rare Met. Mater. Eng.* **2017**, *46*, 28–34. [CrossRef]
15. Suresh, M.; Sharma, A.; More, A.M.; Nayan, N.; Suwas, S. Effect of Scandium addition on evolution of microstructure, texture and mechanical properties of thermo-mechanically processed Al-Li alloy AA2195. *J. Alloys Compd.* **2018**, *740*, 364–374. [CrossRef]

16. Li, H.Z.; Ou, Y.J.; Liao, H.J.; Liang, X.P.; Jiang, J. Microstructural Evolution of High Purity Al-Cu-Mg Alloy during Homogenization. *Mater. Sci. Forum* **2014**, *788*, 208–214. [CrossRef]
17. Gazizov, M.; Teleshov, V.; Zakharov, V.; Kaibyshev, R. Solidification behaviour and the effects of homogenisation on the structure of an Al–Cu–Mg–Ag–Sc alloy. *J. Alloys Compd.* **2011**, *509*, 9497–9507. [CrossRef]
18. Nayan, N.; Narayana Murty, S.V.S.; Jha, A.K.; Pant, B.; Sharma, S.C.; George, K.M.; Sastry, G.V.S. Processing and characterization of Al–Cu–Li alloy AA2195 undergoing scale up production through the vacuum induction melting technique. *Mat. Sci. Eng. A* **2013**, *576*, 21–28. [CrossRef]
19. Fink, D.; Hnatowicz, V.; Kvitek, J.; Havranek, V.; Zhou, J.T. External oxidation of aluminium-lithium alloys. *Surf. Coat. Technol.* **1992**, *51*, 57–64. [CrossRef]
20. Xu, P.; Jiang, F.; Tang, Z.; Yan, N.; Jiang, J.; Xu, X.; Peng, Y. Coarsening of Al3Sc precipitates in Al-Mg-Sc alloys. *J. Alloys Compd.* **2019**, *781*, 209–215. [CrossRef]
21. Royset, J.; Ryum, N. Scandium in aluminium alloys. *Int. Mater. Rev.* **2013**, *50*, 19–44. [CrossRef]
22. Clouet, E.; Lae, L.; Epicier, T.; Lefebvre, W.; Nastar, M.; Deschamps, A. Complex precipitation pathways in multicomponent alloys. *Nat. Mater.* **2006**, *5*, 482–488. [CrossRef] [PubMed]
23. Wang, Y.; Xiong, B.; Li, Z.; Zhang, Y.; Teng, H. Precipitation Behavior of Al3(Sc,Zr) Particles in High-Alloyed Al–Zn–Mg–Cu–Zr–Sc Alloy during Homogenization. *Arab. J. Sci. Eng.* **2021**, *46*, 6027–6037. [CrossRef]
24. Fuller, C.B.; Murray, J.L.; Seidman, D.N. Temporal evolution of the nanostructure of Al(Sc,Zr) alloys: Part I—Chemical compositions of Al3(Sc1−xZrx) precipitates. *Acta Mater.* **2005**, *53*, 5401–5413. [CrossRef]
25. DePottey, A.; Jiang, L.; Dorin, T.; Wood, T.; Langan, T.; Sanders, P. Effect of Cooling Rate on W-Phase Formation in Al-Cu-Sc Alloys. In Proceedings of the TMS Annual Meeting and Exhibition Light Metals 2023, San Diego, CA, USA, 19–23 March 2023. [CrossRef]
26. Li, S.; Jiang, T.; Wang, J.; Chen, L.; Wei, B.; Li, Y.; Xu, G.; Wang, Z. Effects of different external fields on the microstructure and mechanical properties of novel Al-Cu-Li alloy during twin-roll casting. *Mat. Sci. Eng. A* **2019**, *757*, 14–22. [CrossRef]
27. Li, S.; Wei, B.; Yu, C.; Li, Y.; Xu, G.; Li, Y. Evolution of microstructure and properties during homogenization of the novel Al–Li alloy fabricated by electromagnetic oscillation twin-roll casting. *J. Mater. Res. Tech.* **2020**, *9*, 3304–3317. [CrossRef]
28. Grydin, O.; Stolbchenko, M.; Schaper, M.; Belejova, S.; Kralik, R.; Bajtosova, L.; Krivska, B.; Hajek, M.; Cieslar, M. New Twin-Roll Cast Al-Li Based Alloys for High-Strength Applications. *Metals* **2020**, *10*, 987. [CrossRef]
29. Wang, Y.; Wu, G.; Zhang, L.; Guo, Y.; Wang, C.; Li, L.; Xiong, X. Microstructure evolution and mechanical properties of a cast and heat-treated Al–Li–Cu–Mg alloy: Effect of cooling rate during casting. *Mat. Sci. Eng. A* **2023**, *880*, 145366. [CrossRef]
30. MacRae, C.M.; Hughes, E.A.; Laird, J.S.; Glenn, A.M.; Wilson, N.C.; Torpy, A.; Gibson, M.A.; Zhou, X.; Birbilis, N.; Thompson, G.E. An Examination of the Composition and Microstructure of Coarse Intermetallic Particles in AA2099-T8, Including Li Detection. *Microsc. Microanal.* **2018**, *24*, 325–341. [CrossRef]
31. Slamova, M.; Karlik, M.; Rabaut, F.; Slama, P.; Veron, M. Differences in microstructure and texture of Al–Mg sheets produced by twin-roll continuous casting and by direct-chill casting. *Mater. Charact.* **2002**, *49*, 231–240. [CrossRef]
32. Bajtosova, L.; Grydin, O.; Stolbchenko, M.; Schaper, M.; Krivska, B.; Kralik, R.; Slapakova, M.; Cieslar, M. Phase identification in twin-roll cast Al-Li alloys. In Proceedings of the 31st International Conference on Metallurgy and Materials, METAL 2022, Brno, Czech Republic, 18–19 May 2022.
33. Kim, J.-H.; Yeun, J.-H.; Chun, H.-J.; Lee, R.-J.; Too, J.-T.; Yoon, J.-H.; Lee, H.-S. Effect of precipitates on mechanical properties of AA2195. *J. Alloys Compd.* **2016**, *669*, 187–198. [CrossRef]
34. Jin, Y.; Yu, H. Enhanced formability and hardness of AA2195-T6 during electromagnetic forming. *J. Alloys Compd.* **2022**, *890*, 161891. [CrossRef]
35. Sahoo, S.; Ghosh, S. Microstructure evolution of eutectic Al–Cu strips by high-speed twin-roll strip casting process. *Appl. Phys. A Mater.* **2015**, *121*, 45–50. [CrossRef]
36. Zhang, Y.; Wang, J.; Chen, D.; Wang, B.; Zhang, C.; Wang, Z. Effects of cooling rates on microporosity in DC casting Al-Li alloy. *China Foundry* **2022**, *19*, 177–190. [CrossRef]
37. Zhang, F.; Shen, J.; Yan, X.; Sun, J.; Sun, X.; Yang, Y. Homogenization heat treatment of 2099 Al–Li alloy. *Rare Met.* **2013**, *33*, 28–36. [CrossRef]
38. Flemings, M.C. Solidification Processing. *Met. Trans.* **1974**, *5*, 2121–2134. [CrossRef]
39. Ramirez-Vidaurri, L.E.; Castro-Roman, M.; Herrera-Trejo, M.; Fraga-Chavez, K. Secondary dendritic arm spacing and cooling rate relationship for an ASTM F75 alloy. *J. Mater. Res. Technol.* **2022**, *19*, 5049–5065. [CrossRef]